Journal of
Materials Chemistry C

ROYAL SOCIETY
OF CHEMISTRY

PAPER

View Article Online
View Journal | View Issue

Check for updates

Cite this: *J. Mater. Chem. C*, 2025, **13**, 16067

Insights into light transmission through 2,5-bis(arylethynyl)pyrazine based crystals: a combined experimental and theoretical study†

Irene Chacón-Jiménez,[a] Juan Sánchez-Rincón,[b] Berta Gómez-Lor,[c] M. Victoria Gomez,[a] Juan Cabanillas-González,[d] M. Carmen Ruíz Delgado,[b] Iván Torres-Moya,*[a] Ana M. Rodríguez*[a] and Pilar Prieto*[a]

Received 11th March 2025,
Accepted 22nd June 2025

DOI: 10.1039/d5tc01067e

rsc.li/materials-c

In the field of optical nano/micro waveguides, the ability to modulate the crystal structure and understand the relationship between structure and waveguide properties is a crucial aspect of significant interest. These factors play a vital role in the design of materials capable of transmitting light with the highest possible efficiency. In this work, crystals and co-crystals based on 2,5-bis(arylethynyl)pyrazines have been synthesized. The introduction of functional groups of diverse electronic nature in different positions, as well as the formation of co-crystals with 1,4-diiodotetrafluorobenzene (F_4DIB) as a co-assembler, enabled crystalline structures with different morphologies and good optical waveguide properties to be obtained. Additionally, aspects of paramount importance in light transmission have been studied, including morphology, crystal parameters such as packing arrangement, aggregate types, intermolecular distances, the presence of microchannels in the crystal, and the relationship between the direction of the molecular transition dipole moment and the propagating electric field.

Introduction

The ability to transmit data through light has revolutionized communication, enabling the development of the Internet. However, this progress has not yet been implemented at the microscopic scale. The development of integrated photonic devices in the nano/micro scale, where photons play the role of charge carriers, could advance communication technologies in conjunction with developments in organic optoelectronic devices such as field effect transistors,[1] LEDs,[2] sensors, and photodetectors.[3] Photonic circuits could address fundamental limitations of electronics, including energy consumption and speed.[4] A key component in a photonic device is the optical waveguide, a physical structure that confines and transmits light with minimal losses, analogous to an electronic wire in electronic devices.[5] In recent decades, conjugated molecules have emerged as promising building blocks for nano/micro waveguides.[6–9] These organic waveguides offer advantages over inorganic ones, such as simple fabrication by self-assembly into well-ordered defect-free crystals, thermal stability, solution processability, and in some cases high photoluminescence (PL) efficiency. It is worth mentioning that their optical properties can be tuned by adjusting molecular structures and doping, which alters their physical characteristics.[10] Recent studies have highlighted organic waveguides with novel properties such as chirality,[11] anisotropy,[12] flexibility,[13] and stimulus-responsiveness,[14–16] making them suitable for real-world applications.

In this sense, co-crystals,[17] formed by two or more chemical compounds through non-covalent interactions (*e.g.*, π–π, hydrogen, or halogen bonds), are useful tools for modifying supramolecular architectures. Since Wöhler's discovery of the first co-crystal in 1844[18] and its definition in 2003,[19–21] organic co-crystals have gained attention for their role in optoelectronic devices. They offer tunable luminescence, solution processability, controllable phases, and adjustable size, morphology and molecular packing, which can improve optoelectronic properties through crystal engineering.[22]

---

[a] *Department of Inorganic, Organic Chemistry and Biochemistry, Faculty of Chemical Science and Technologies, University of Castilla-La Mancha (UCLM)-IRICA, 13071 Ciudad Real, Spain. E-mail: MariaPilar.Prieto@uclm.es, AnaMaria.RFdez@uclm.es, Ivan.torresmoya@uclm.es*

[b] *Department of Physical Chemistry, University of Málaga, Campus de Teatinos s/n, 29071 Málaga, Spain*

[c] *Institute of Materials Science of Madrid (ICMM-CSIC), Sor Juana Inés de la Cruz 3, Cantoblanco, 28049 Madrid, Spain*

[d] *Madrid Institute for Advanced Studies, IMDEA Nanociencia, Calle Faraday 9, Ciudad Universitaria de Cantoblanco, 28049 Madrid, Spain*

† Electronic supplementary information (ESI) available. CCDC 2386785 (**1a**), 2386786 (**1b**), 2386787 (**Co-1b**), 2386788 (**1c**), 2386789 (**1d**) and 2386790 (**Co-1d**). For ESI and crystallographic data in CIF or other electronic format see DOI: https://doi.org/10.1039/d5tc01067e

Two effective strategies for tailoring optical properties of co-crystals are (i) the use of directional halogen bonds, which provide higher crystal robustness than hydrogen bonds,[23] and (ii) charge transfer (CT) interactions to modulate the optoelectronic performance.[24] Co-crystals, formed by halogen bonds as acceptors and molecules with nitrogen-containing lone pairs as donors, are especially promising for combining these properties. The most commonly acceptor employed in the formation of co-crystals is 1,4-diiodotetrafluorobenzene (F_4DIB).[25]

Understanding how light interacts with crystal structures or how the structure influences light guiding is critical for designing materials with enhanced photonic properties. For these reasons, an in-depth understanding of the structure–property relationship is of paramount importance.

In some organic nanowires, light is transmitted not only according to Schell's law but also *via* the exciton–polariton (EP) mechanism.[26] Several structural factors influence exciton–photon interactions and light guiding: (i) crystal structure: high crystallinity and short intermolecular distances along the packing direction are essential, with J-type aggregates favoring photonic applications.[27] Meanwhile, we recently observed that internal crystal microchannels enhance optical waveguiding by facilitating the EP mechanism.[28,29] (ii) Interaction with the electric field: polaritons are light–matter quasiparticles influenced by an external electric field (E). Thus, the photon interacts with the transition dipole moment (TDM, μ) due to the overlap of absorption and emission in active materials, the molecular dipole orientation determining the coupling strength.[30] (iii) Exciton stability: an external electric field can reduce exciton stability. Charge transfer (CT) Frenkel excitons in highly ordered organic crystals with high energy binding are particularly promising.[31] While some studies address individual factors, few investigate their interrelations, making this a key focus of our research.

Considering all the aforementioned factors, the main objective of this paper is to study the optical waveguide behavior of various 2,5-bis(arylethynyl)pyrazine derivatives and their co-crystals with 1,4-diiodotetrafluorobenzene (F_4DIB) (Fig. 1) to gain a deeper understanding of their light-guiding mechanisms. While some studies focus on individual factors, few investigate their interrelations, which is a key focus of our research.

Based on our prior experience in this field, we selected simple molecules that are easily synthesized and extensively modifiable, allowing the introduction of substituents with diverse electronic and structural features. Pyrazines[32] were chosen as the core because among six-membered nitrogen heterocycles they are one of the most frequently used to form crystalline halogen-bonded adducts.[33]

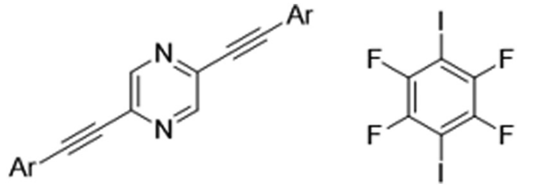

Fig. 1 Chemical structure of 2,5-bis(arylethynyl)pyrazines (left) and the co-assembler 1,4-diiodotetrafluorobenzene (F_4DIB) (right), object of study in this work.

The knowledge gained from this work could contribute to the development of materials with improved photonic properties, tailored on a custom-made basis.

Results and discussion

Design, synthesis and characterization of molecules

As mentioned above, in this work we have studied the optical properties of crystals and co-crystals of 2,5-bis(arylethynyl)-pyrazine derivatives. The choice of this core lies on the one hand, in its structural simplicity that can influence the formation of high-quality crystals, and, on the other hand, its electron-accepting nature, which enables the modulation of the electronic properties of the system. Additionally, the electron pairs located on the nitrogen atoms allow the formation of nitrogen–halogen bonds, necessary for forming co-crystals. Triple bonds are introduced to favor packing through C–H$\cdots\pi$ interactions[34] and flexibility,[35] as well as $-CF_3$ and –OMe groups in different positions, since it has been shown that their presence allows the formation of crystalline structures by enhancing the formation of hydrogen bonds.[28]

A simple synthesis was performed, adhering to the principles of sustainable chemistry, using commercial reagents in a single reaction step. Additionally, microwave radiation was employed as the energy source, leading to a significant reduction in reaction time, a substantial increase in selectivity and yield, and considerable energy savings.[36–38]

Hence, 2,5-bis(arylethynyl)pyrazine derivatives (**1a–d**) were synthesized *via* Sonogashira C–C cross-coupling between 2,5-dibromopyrazine (**2**) and the corresponding arylethynyl derivatives (**3a–d**). The reactions were carried out under an inert atmosphere using PdEncat as a reusable catalyst, CuI as a co-catalyst, DBU as a base, and a small amount of CH_3CN (1 mL) as the solvent (Scheme 1).[39,40] All compounds were purified using column chromatography on silica gel employing hexane/ethyl acetate 9 : 1 as an eluent reporting satisfactory analytical NMR spectroscopy and MS data (see Fig. S1–S26, ESI†). The higher yields observed for *ortho*-substituted are likely due to steric and conformational effects that enhance catalyst interaction and reduce side reactions, such as Glaser coupling.

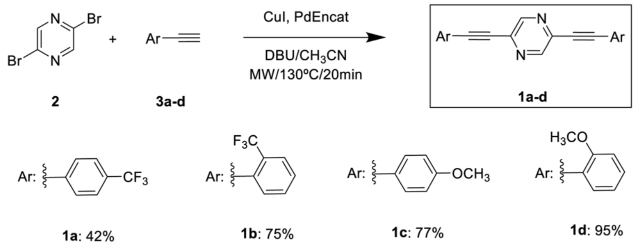

Scheme 1 Synthetic procedure for the preparation of derivatives **1a–d**.

Electronic effects alone cannot explain this trend, given the opposing nature of the substituents involved.

Theoretical analysis of the conformational and electronic structure

A conformational study of compounds **1a–d** was carried out using the density functional theory (DFT) method at the ωB97XD/6-31G** level. The most stable conformer for each compound is also depicted in Fig. 2. As shown, the ground electronic state potential energy hypersurface reveals the presence of four minimum-energy conformers with relative energy differences of less than 2.35 kcal mol^{-1}. This highlights the conformational flexibility imparted by the triple bonds. This is also supported by the low activation energies among the conformers, which are less than 3.24 kcal mol^{-1}, that is thermally inter-convertible (Fig. S27–S30, ESI†). It is noteworthy that the *para*-substituted compounds exhibit greater flexibility than the *ortho*-substituted ones. Additionally, the compounds with $-CF_3$ in the *ortho* position present more difficulty in rotating compared to their –OMe substituted analogues, probably due to the close interaction between the fluorine atoms and the hydrogen atoms of the central pyrazine units (*i.e.*, calculated at 3.30 Å which is only moderately larger than the sum of the van der Waals radii which is 2.67 Å).

DFT-calculated topologies of HOMO and LUMO orbitals and HOMO–LUMO gap values for **1a–d** compounds and the unsubstituted homologue model systems taken as the reference (named as the core) are displayed in Fig. 3 (see Fig. S31 and S32 for the results obtained at the B3LYP/6-31G** and ωB97XD/LanL2DZ levels of theory, respectively, ESI†). The HOMO and LUMO orbitals are delocalized throughout the entire molecule, indicating the favorable conjugation of these systems. However, differences arise depending on the substitution profile. In $-CF_3$-substituted systems (**1a** and **1b**), a similar stabilization of the HOMO and LUMO orbitals occurs, resulting in no significant change in the HOMO–LUMO gap (7.13 eV) compared to the unsubstituted core model molecule. However, in the compounds with –OMe substituents (**1c** and **1d**), there is a greater destabilization of the HOMO orbital compared to that of the LUMO, resulting in a decrease of the HOMO–LUMO gap with respect to the unsubstituted compound (6.91 eV in **1c** and 6.97 eV in **1d** *versus* 7.13 eV in the reference core systems). This can be attributed to the donor character of the methoxy groups, which results in greater delocalization of the HOMO orbitals over the outer phenyl rings, while the LUMO orbitals are more

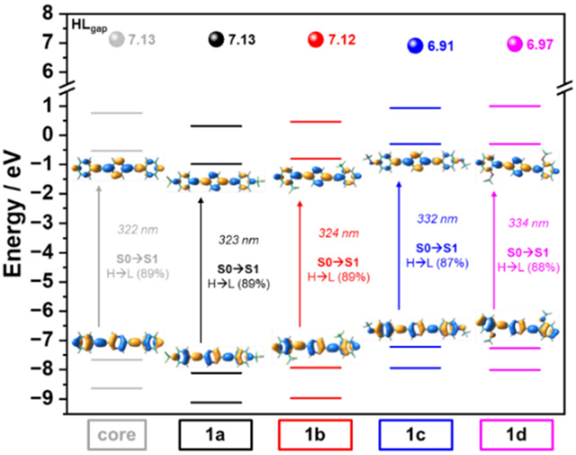

Fig. 3 DFT-calculated frontier molecular orbital energies and topologies (ωB97X-D/6-31G** level) for **1a–d** derivatives and the reference molecule without substituents (named as the core). The $S_0 \rightarrow S_1$ electronic transitions are also shown.

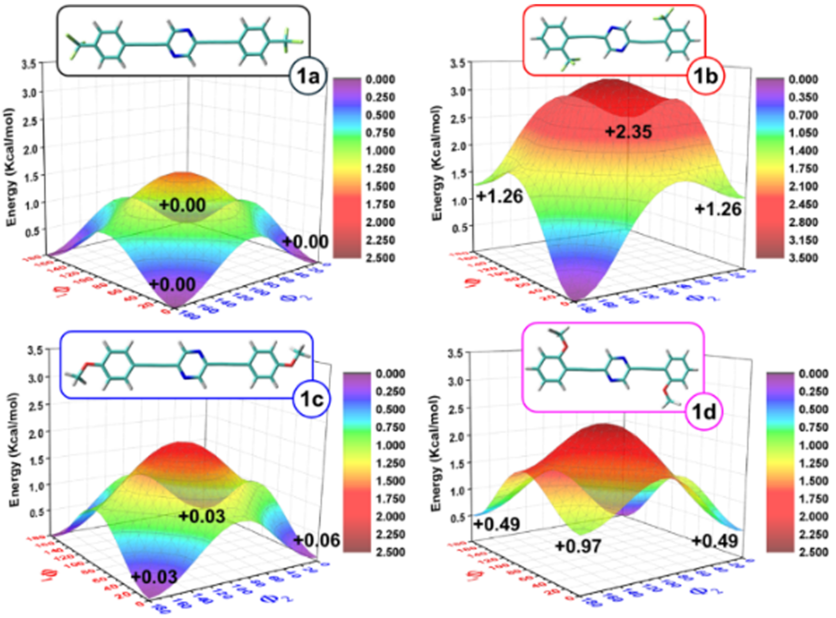

Fig. 2 Potential energy hypersurface $E = E(f_1, f_2)$, in terms of f_1, f_2 which refer to the dihedral angles between the pyrazine unit and the lateral phenyl rings, for **1a–d** compounds computed at the ωB97X-D/6-31G** level of theory. The most stable conformer for each compound is also presented.

localized on the central pyrazine and adjacent acetylene groups. This effect is more pronounced in compound **1c**, as the *para*-substitution of the methoxy groups facilitates a more extensive π-conjugation.

New calculations were carried out using the LanL2DZ basis set, for the study of the co-crystals. The results confirm that the electron density of the frontier orbitals in **Co-1b** and **Co-1d** is localized on the pyrazine unit, and that the presence of the co-assembler leads to a slight decrease in the HOMO–LUMO gap (Fig. S33, ESI†).

Time-dependent DFT (TD-DFT) vertical excitation energies predict that the lowest energy electronic transition $S_0 \rightarrow S_1$ in all systems is associated with a HOMO → LUMO one-electron excitation (Fig. 3). Therefore, the UV-Vis absorption maxima are expected to be bathochromically shifted for compounds with –OMe groups (**1c–d**), with this effect being more pronounced for *para*-substituted compounds. It is worth noting that this trend is also preserved in the TD-DFT calculations obtained including the solvent effects (in $CHCl_3$ and DMF, see Fig. S34 and S35, ESI†).

Photophysical properties

The absorption and photoluminescence spectra of derivatives **1a–d** in solution were recorded in hexane, toluene, chloroform, dichloromethane, tetrahydrofuran, acetone, methanol and dimethylformamide at a concentration of 10^{-5} M upon photo-exciting the samples at the absorption maxima of the lowest energy band. The most relevant data are summarized in Fig. 4 and Fig. S36, S37 (ESI†).

The UV-Vis absorption spectra (Fig. 4a and c) indicate that the compounds with –OMe substituents (**1c–d**) exhibit a bathochromic shift compared to their $-CF_3$ analogues (**1a–b**) across all the solvents, due to their D–A–D (donor–acceptor–donor) character which results in a lower HOMO–LUMO gap (Fig. S34 and S35, ESI†). Moreover, the electronic localization in the *para*-substituted derivatives is more effective than the *ortho*-substituted ones, resulting in a bathochromic shift in the former. This effect is particularly relevant in the –OMe derivatives. These experimental results agree very well with the theoretical calculations presented above.

Additionally, we have recorded the solid-state absorption spectra for all compounds. Compared to the solution spectra, which displays more defined bands due to molecular dispersion, the solid-state spectra show broader features and additional bands, likely resulting from enhanced intermolecular interactions. It can be pointed out that for the co-crystals **Co-1b** and **Co-1d**, a distinct absorption band appears around 600 nm, which may be associated with aggregation effects or specific electronic interactions between the pyrazine derivative and the co-assembler in the solid state (Fig. S41, ESI†).

In contrast, the emission spectra (Fig. 4b and d) show significant differences depending on the solvent used. In halogenated and polar protic solvents (CH_2Cl_2, $CHCl_3$ and MeOH) a similar trend is observed in both absorption and emission spectra, with the –OMe derivatives exhibiting a bathochromic shift compared to the $-CF_3$ derivatives (Fig. S36, ESI†). In contrast, in apolar and polar aprotic solvents (hexane, toluene, THF, acetone and DMF), the behavior differs, with the emission wavelengths being nearly identical for all compounds (Fig. S37, ESI†). It is well-established that, in donor–acceptor systems, solvent properties strongly influence the excited states of molecules, stabilizing them through various interactions, such as solvation, dipole–dipole interactions, and hydrogen bonding.[41] In this case, stabilization in protic solvents like methanol or halogenated solvents is likely due to hydrogen bond formation.

Photoluminescence (PL) lifetimes were measured in both solution and solid state for all derivatives (Table S1, ESI†). The methoxy-substituted compounds (**1c** and **1d**) exhibited longer PL lifetimes than the trifluoromethyl analogues (**1a** and **1b**), indicating reduced non-radiative deactivation. This difference

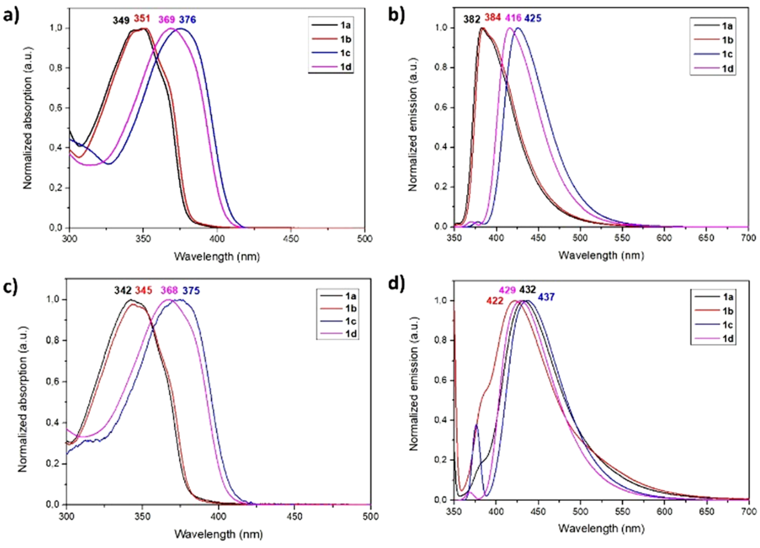

Fig. 4 Absorption and emission spectra of **1a–d** $CHCl_3$ solutions (1×10^{-5} M) (a) and (b) and in DMF solution (1×10^{-5} M) (c) and (d).

is likely due to the electronic nature of the substituents: the methoxy group (–OCH_3) is an electron donor that can stabilize excited states and minimize non-radiative decay pathways, while the trifluoromethyl group (–CF_3), a strong electron acceptor, may enhance non-radiative processes by increasing polarity and structural rigidity. These effects could promote vibrational interactions that facilitate internal conversion or intersystem crossing. No significant differences were observed between compounds **1b** and **1d** and their respective co-crystals (**Co-1b** and **Co-1d**) (Table S1, ESI†).

Quantum yields both in solution and in solid state were also calculated for all the derivatives, detecting slightly higher values for methoxy-substituted compounds (**1c** and **1d**) compared to those with trifluoromethyl groups (**1a** and **1b**). Co-crystals **Co-1b** and **Co-1d** showed the highest quantum yields in the solid state (Table S1, ESI†). The improved efficiency in methoxy derivatives is likely due to the electron-donating nature of the methoxy group, which stabilizes excited states and reduces non-radiative decay. Additionally, the co-crystals benefit from intermolecular interactions that rigidify the structure and suppress non-radiative pathways, leading to enhanced fluorescence compared to the isolated pyrazine derivatives.

The solvatochromic properties of these compounds (Fig. S40 and Table S2, ESI†)[42] are in line with the distribution of charges theoretically obtained which predict a larger polarization (that is, a higher D–A–D character) in the S_1 excited state when compared to the S_0 ground state (Fig. S42, ESI†). Interestingly, the charge polarization is greater in the *para*-substituted compounds due to their more favorable electronic delocalization along the chain when it occurs in a linear fashion, as well as in the methoxylated derivatives (**1c** and **1d**) due to their more pronounced D–A–D character. Remarkably, among all systems, the highest polarization is predicted for the *para*-OMe **1c** compound (Fig. S40, ESI†), which has the highest bathochromic shift within the series (*i.e.*, 78 nm).

Molecular assembly

Crystals of **1a–d** were obtained using the slow diffusion technique, which relies on the gradual exchange of vapors between a good solvent and a bad one. In this sense, we chose the different good and bad solvents as a function of the solubility of derivatives **1a–d** in $CHCl_3$, THF, CH_3CN, hexane, MeOH and EtOH (Table S3, ESI†). The morphology of the resulting aggregates was examined using high-resolution scanning electron microscopy (HRSEM). It is known that solvent nature is one of the most important parameters in this process. The solvent mixtures that yielded the best crystal morphology were THF/CH_3CN for **1a**, THF/EtOH for **1b**, and $CHCl_3$/MeOH for **1c** and **1d** (Fig. 5). It is worth noting that in the case of compound **1d**, amorphous structures and twinning were obtained, making it necessary to test new solvent mixtures. Thus, various solvent mixtures, where the compound is both soluble and insoluble, were used as poor solvents, with $CHCl_3$/$CHCl_3$: MeOH (20 : 80) being the optimal mixture in which well-formed crystalline structures were identified. The best morphology was achieved with compound **1b** (Fig. 5b). Using this as a model, factors such as temperature, time, concentration, and solvent ratio were optimized to modulate the molecular self-assembly process and the properties of the resulting materials (Tables S4 and S5, ESI†). The results indicated that the optimal temperature was 21 °C, the optimal concentration was 1 mg mL^{-1}, and no significant effect was observed when varying the amount of poor solvent. Additionally, it was noted that as the concentration increased, fibers were formed earlier and exhibited greater thickness.

In general, the *para*-substituted compounds **1a** and **1c** showed crystals with a lamellar morphology of about 1 mm in length and 700 μm in width for **1a** and 1 mm in length and 0.7 mm in width for **1c**, while *ortho*-substituted compounds **1b** and **1d** show well-defined needle-shaped crystals of approximately 3 mm in length and 800 μm in width for **1b** and 2 mm in length and 500 μm in width for **1d** (Fig. 5).

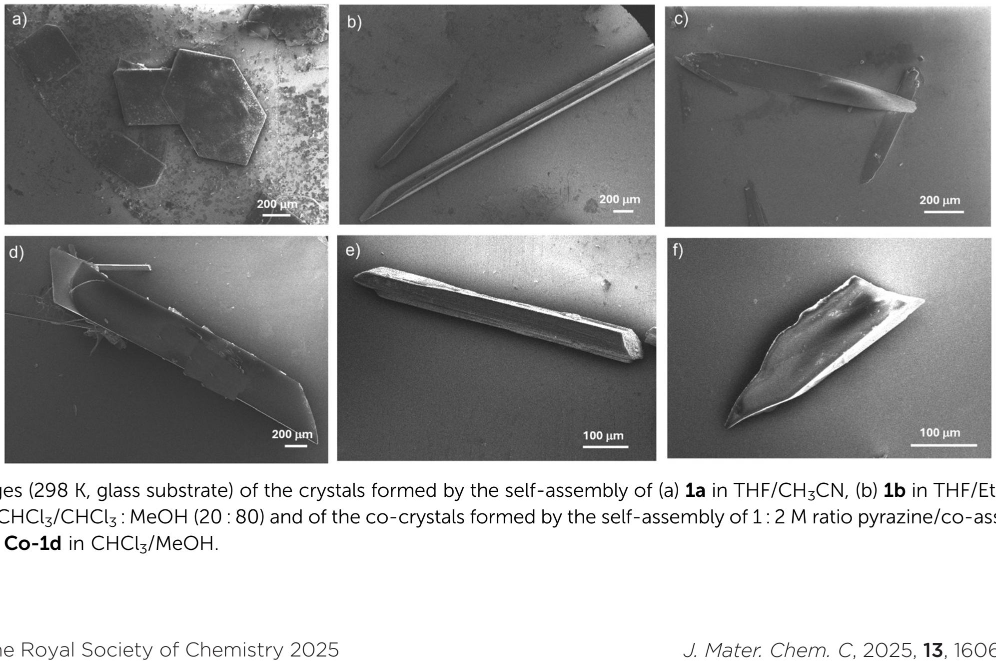

Fig. 5 HRSEM images (298 K, glass substrate) of the crystals formed by the self-assembly of (a) **1a** in THF/CH_3CN, (b) **1b** in THF/EtOH, (c) **1c** in $CHCl_3$/MeOH and (d) **1d** in $CHCl_3$/$CHCl_3$: MeOH (20 : 80) and of the co-crystals formed by the self-assembly of 1 : 2 M ratio pyrazine/co-assembler of (e) **Co-1b** in THF/EtOH and (f) **Co-1d** in $CHCl_3$/MeOH.

Co-crystallization

As mentioned above, the co-crystallisation technique allows the customised design and synthesis of new multifunctional materials with novel photophysical properties based on the modification of the non-covalent intermolecular interactions that comprise them.[43]

Based on the results reported in the literature about co-crystal formation, two hybrid methods were developed.[44] In both, influential parameters for crystal formation such as temperature, sonication and concentration of the species involved are varied.

Two of the co-assemblers with the best properties described in the literature, 1,4-diiodotetrafluorobenzene (F_4DIB)[25,45] and 4-bromo-2,3,5,6-tetrafluorobenzene acid (BTFBA),[45,46] were employed allowing the modulation of crystal morphology through the formation of strong directional halogen–heteroatom bonds and hydrogen bonds. In this way, a change in the crystal structure can induce significant changes in the final properties of the material.

The optimisation of the co-crystal formation conditions is presented in the ESI† (Tables S6 and S7). Only co-crystals of the *ortho*-substituted derivatives with F_4DIB were obtained, designated as **Co-1b** and **Co-1d**, respectively. This indicates the greater ability of nitrogen to form N–I bonds rather than hydrogen bonds, as well as the importance of the functional group position. The procedure to find the optimal conditions consisted in dissolving the compound and the co-assembler in a 1 : 2 M ratio at 40 °C for 30 min in the good solvent, followed by the slow diffusion procedure described above. In addition, in the case of **Co-1d** it was necessary to use sonication to obtain the co-crystal. The as-prepared crystals can be observed in Fig. 5.

Co-1b shows a defined fibrillar morphology of about 600 μm in length and 60 μm in width, while **Co-1d** shows a 2D lamellar morphology of about 450 μm in length and 120 μm in width. As observed, the presence of a co-assembler allows the variation in the crystal shape. In the case of **1d**, the crystal of the individual molecule has a 1D fibrillar structure, whereas the co-crystal **Co-1d** has a 2D morphology.

As expected, introducing different substituents at various positions leads to the formation of distinct crystal forms. Additionally, co-crystallization facilitates alterations in crystal morphology of the crystal in comparison to the isolated molecule.

X-ray structure determination

The structures of crystals based on **1a–d**, **Co-1b** and **Co-1d** were successfully resolved by single crystal X-ray diffraction. Fig. 6 shows the molecular unit with the adopted atom-numbering. Crystallographic data and the most relevant interactions are provided in Section S7 of the ESI† (Tables S8, S9 and Fig. S46–S48, ESI†).

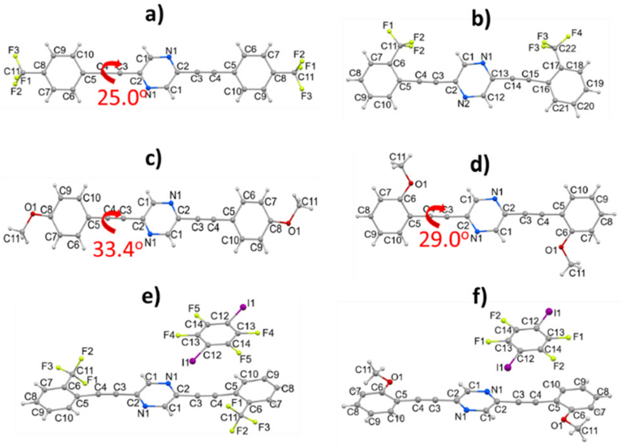

Fig. 6 The molecular unit for (a) **1a**, (b) **1b**, (c) **1c**, (d) **1d**, (e) **Co-1b** and (f) **Co-1d** compounds, showing the adopted atom-numbering scheme. For the non-planar structures, the dihedral angles between the phenyl rings and the central pyrazine ring are also shown.

A comparison of the geometries reveals that derivatives **1a**, **1c**, and **1d** exhibit non-planar structures where the phenyl rings are rotated relative to the central pyrazine ring at angles ranging from 25° to 33° (Fig. 6a, c and d). In contrast, derivative **1b** and the two co-crystals display a fully coplanar arrangement of the phenyl rings with respect to the pyrazine core (Fig. 6b, e and f). The introduction of the co-assembler into **1d** induces a change in the planarity of the molecule which is attributed to the significant steric hindrance exerted by the co-assembler as well as the strong directionality of the N···I halogen bonds and F···H interactions (Fig. 6d *vs.* Fig. 6f). Experimental data show that the two –OMe groups of the molecule in **1d** exhibit a *trans*-orientation relative to the molecular plane whereas in **1b** the $-CF_3$ groups are oriented in the same side of the molecule (*cis*-orientation). In addition, the introduction of the bulky co-assembler in derivative **1b** induces a twisting of the Ph–CF_3 rings, resulting in a *trans*-orientation for these substituents.

The study of the packing arrangements in the 2,5-bis-(arylethynyl)pyrazine derivatives reveals that all structures are stabilised by hydrogen bonds between the nitrogen atom of the pyrazine ring and either the H_{ortho} or H_{meta} hydrogen atoms of both Ph–CF_3 and Ph–OMe rings (Table S10, ESI†).

Different packing modes can be observed for these compounds. The *para*-derivatives (**1a** and **1c**) exhibit a very similar structural arrangement (Fig. S46, ESI†) where each molecule is surrounded by six adjacent molecules through CH···π interactions between the hydrogen atom of the pyrazine ring and the triple bonds of neighbouring molecules. In the case of **1c**, these interactions are further strengthened by additional CH···π interactions between the –OMe groups and the triple bonds. The extension of these interactions results in a lamellar packing arrangement that extends in the *bc* plane for **1a** and in the *ab*-plane for **1c**. Similarly, the *ortho*-substituted derivatives (**1b** and **1d**) exhibit a comparable packing arrangement where the molecules are predominantly connected by hydrogen bonds (Fig. S47 and Table S10, ESI†). The molecules of compounds **1b** and **1d** are able to stack along the [010] and [100] directions respectively with intermolecular π···π stacking interactions resulting in a herringbone stacking. For the co-crystals **Co-1b** and **Co-1d**, the F_4DIB molecules act as linkers for the **1b** or **1d** molecules through N···I halogen bonding and CH···F interactions (Fig. S48–S50, ESI†), resulting in the formation of extended sheets in the (−1−13) plane. Finally, a 2D lamellar network is obtained for both compounds driven by different π···π interactions (Table S10, ESI†).

Fig. 7 illustrates the different crystal morphologies exhibited by these derivatives. In order to rationalize a method for modulating the final morphology of a crystal, it is essential to investigate the dominant interactions that govern the crystallization process. In this context, we have observed that changing the substituents from the *para*- to the *ortho*-position leads to a change in the crystal morphology due to a change in the intermolecular interactions. When a crystal has a stronger interaction such as π···π in one direction compared to others it tends to grow preferentially along this direction leading to a one-dimensional 1D nanowire morphology. In contrast, when interactions of comparable strength such as CH···π interactions are present in two or more directions, the crystals typically adopt two-dimensional 2D or 3D morphologies as no single direction dominates the growth process.

Thus, in the *para*-derivatives **1a** and **1c**, no dominant directional interactions are observed, and the crystal packing is mainly influenced by weak CH···π interactions extending along the [100] and [010] directions, resulting in a 2D lamellar morphology (Fig. S51a and c, ESI†). In contrast, the positional change of the substituent in the *ortho*-derivatives **1b** and **1d** prevents the formation of CH···π interactions and favors the development of stronger π···π interactions in a specific direction ([010] for **1b** and [100] for **1d**) (Fig. S51b and d, ESI†). These strong directional π···π interactions drive crystal growth along the respective directions leading to the formation of 1D needle-like morphologies.

In the case of the co-crystals, both exhibit dominant π···π interactions, but **Co-1b** forms a 1D needle-like morphology, while **Co-1d** adopts a 2D lamellar morphology (Fig. 5). To account for these differences, it is necessary to carefully analyse their interactions. For **Co-1b**, the strong π···π interactions mainly involve the triple bonds of the 2,5-bis(arylethynyl)pyrazine molecule and the Ph–CF_3 or pyrazine rings of neighbouring molecules along the [100] direction (Fig. S52a, ESI†). The co-assembler interacts with the 2,5-bis(arylethynyl)pyrazine molecule *via* CF···π interactions, which are comparatively weaker, leading to crystal growth predominantly along the π···π stacking in the [100] direction resulting in a 1D wire morphology.

In contrast, in the co-crystal **Co-1d**, π···π interactions are not formed between the triple bonds and the molecules are instead displaced relative to each other. The interactions occur between the Ph–OMe, pyrazine and F_4DIB rings and extend along the *bc* plane (Fig. S52b, ESI†). In this structure, each 2,5-bis(arylethynyl)pyrazine molecule is involved in π···π interactions with two other 2,5-bis(arylethynyl)pyrazine molecules and two co-assembler molecules (F_4DIB) resulting in crystal growth predominantly along the (100) plane. This interaction pattern leads to the formation of the expected 2D lamellar morphology.

The packing pattern of crystal **1b** is remarkably similar to that of the well-studied 9,10-bis(phenylethynyl)anthracene (BPEA),

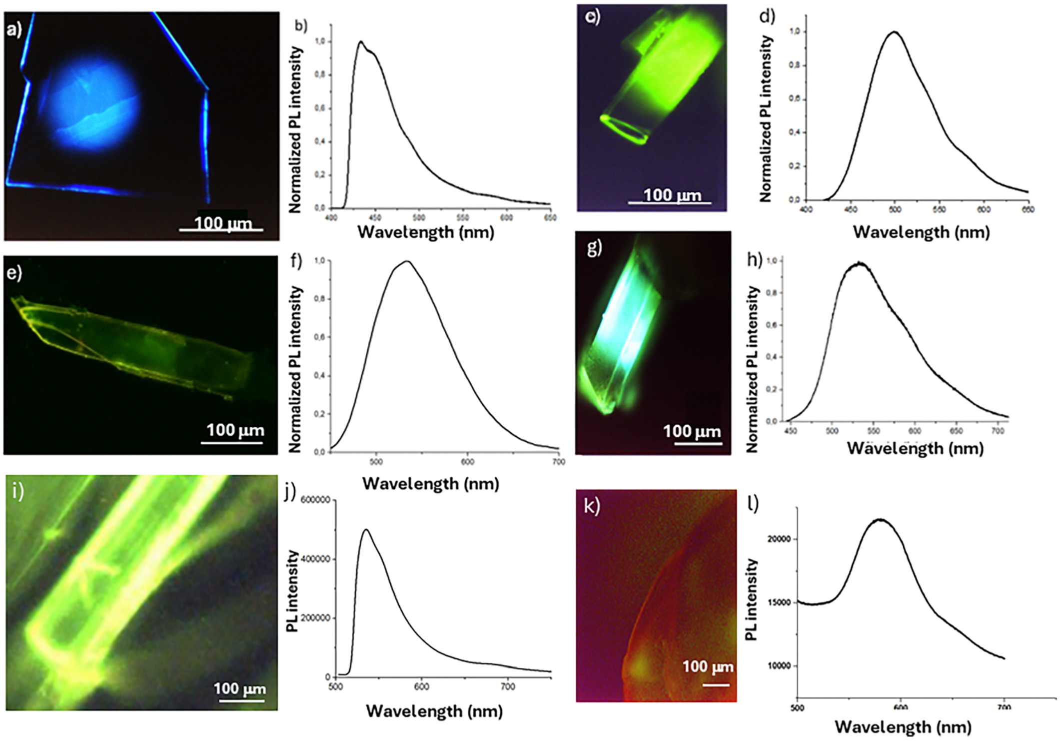

Fig. 7 Photoluminescence (PL) microscopy images of (a) **1a**, (c) **1b**, (e) **1c**, (g) **1d**, (i) **Co-1b** and (k) **Co-1d**. PL spectra of crystals of (b) **1a**, (d) **1b**, (f) **1c**, (h) **1d**, (j) **Co-1b** and (l) **Co-1d**. Crystals were photoexcited at 365 nm.

which exhibits excellent optical waveguide properties due to its cofacial herringbone one-dimensional π-stacking of the conjugated system along the growth direction.[29] In addition, crystal **1b** exhibits a significant number of strongly directional hydrogen bonds (Table S10, ESI†). According to the literature, these bonds play a critical role in guiding the packing, with their number, position, and strength profoundly influencing the self-assembly process and the resulting properties.[47,48]

Optical waveguide properties

The optical waveguiding behavior of the crystals based on compounds **1a–d** and co-crystals (**Co-1b** and **Co-1d**), which exhibited the largest size and best morphologies (Fig. 5), was qualitatively evaluated using confocal fluorescence microscopy.

Photoluminescence (PL) microscopy images and spectra were recorded for all crystals to assess their potential optical waveguiding properties (Fig. 7). Upon photoexcitation at 365 nm, all crystals exhibited luminescence and active optical waveguiding, transmitting light in the 400–600 nm range. Luminescence propagates efficiently along the longitudinal axis, corresponding to the smooth, defect-free structure of the nanowires, as observed in the HRSEM images.

Confocal microscopy images revealed that the *ortho*-substituted derivatives exhibit higher fluorescence intensity compared to the *para*-substituted ones (Fig. 7c and 7g *vs.* Fig. 7a and e). These findings confirm that the superior 1D morphology of the *ortho* derivatives results in more efficient light transmission.

The PL spectra of the crystals show a bathochromic shift in the methoxy derivatives (Fig. 7f and h) compared to the trifluoromethyl derivatives (Fig. 7b and d), attributed to the electron-donating character of the methoxy groups. Specifically, **1a** exhibits weak blue emission centered at 432 nm, while its analogue **1c** shows weak green emission at 532 nm (Fig. 7b *vs.* Fig. 7f), resulting in a 100 nm bathochromic shift. Similarly, the *ortho* derivatives display a bathochromic shift of approximately 40 nm, with **1b** emitting at 501 nm and **1d** at 541 nm (Fig. 7d *vs.* Fig. 7h).

In the case of co-crystals formed between **1b** and **1d** with F_4DIB (**Co-1b** and **Co-1d**), a bathochromic shift is observed in comparison with the individual pyrazine's analogues (Fig. 7). In particular, the co-crystal of **1b** with F_4DIB exhibited green luminescence with a maximum peak centered at 535 nm, showing a bathochromic shift of 34 nm in comparison to **1b**. In the same way, the co-crystal of **1d** with F_4DIB exhibited a broad band centered at 595 nm, with a bathochromic shift of 54 nm due to the co-crystal formation. This behavior explains the change in aggregation, which shifts from H-aggregates in the *ortho*-substituted derivatives to J-aggregates in the co-crystals.

Moreover, in order to evaluate the efficiency of the optical waveguide behavior in the crystals of 2,5-bis(arylethynyl)-pyrazine derivatives obtained, the optical loss coefficients were measured in **1b** and **1c** upon moving the photoexcitation (365 nm) spot along the length of the crystal while detecting the emission at one of the tips (Fig. S44, ESI†). The fluorescence intensity (I_{out}) upon moving the pump a distance x respect to the initial position (I_{in}) is given by the Lambert–Beer law $I_{\text{out}} = I_{\text{in}}e^{-\alpha x}$, where I_{out} and I_{in} are the PL intensities at the output and input, respectively, x is the propagation distance and α is the absorption coefficient in μm^{-1}, which is related to the optical loss coefficient (OLC) α' (dB μm^{-1}) through the equation α' (dB μm^{-1}) $\approx$ 4.34 α (dB μm^{-1}). The α' values for **1b** and **1c** (Fig. S44, ESI†) were 1.78×10^{-3} and 8.16×10^{-3} dB μm^{-1}, respectively. The α' value of the **1b** crystal is lower than some recently reported in optical waveguiding organic crystals[12,49–53] and in the order of the best derivatives reported recently by our research group.[28,54] Unfortunately, for the rest of crystals it was not possible to determine the OLC, since the size of the crystal was not enough due to the limitations of our experimental set-up. The experimental set-up employed for our measurement is recorded in Fig. S45 (ESI†). These results confirm that superior morphology exhibited by **1b** translates into lower optical losses and improved performance as an optical waveguide.

Relation between optical waveguiding and structure

As stated previously in the Introduction section, the transmission of light through crystalline structures is influenced by several aspects. Identifying these aspects helps in designing compounds with improved waveguide properties in a targeted manner, avoiding the trial-and-error method. The main factors are discussed below.

Crystal structure

Crystal quality plays an important role, since smooth surfaces enable total internal reflection and reduced light scattering. Additionally, it is well known that the behavior as active waveguides strongly depends on molecular packing due to the Frenkel exciton generated in highly ordered organic crystals being highly stable. Regarding this aspect, J-aggregates exhibit increased oscillator strength of the highest Frenkel exciton, along with a narrower absorption and photoluminescence band relative to the monomer. This feature, combined with their hyperchromicity, superradiance, and high quantum fluorescence yield, improves the strong light–matter interaction and promotes the potential use of J-aggregates in optoelectronic applications.[27,55] In contrast, in H-aggregates, this interaction is weaker due to their broad spectral linewidth and vibronically rich spectra. This fact, combined with the typically forbidden emission of H-aggregates,[56] limits their applications in optoelectronics. However, recent articles have been published reporting the transmission of light through H-aggregates.[56–58]

It is worth mentioning that the excellent crystallinity and short intermolecular distances (between 3.4 and 3.5 Å) in the packing direction results in a large overlap between adjacent π-orbitals and improves exciton-photon coupling allowing the light-guiding process.[31,55] Additionally, while molecular packing plays a crucial role in exciton migration, the waveguiding properties of a material are more strongly influenced by its geometry.[56]

Alternatively, it is well known that classical J-aggregation refers to the accumulation of molecules in a slip face-to-face

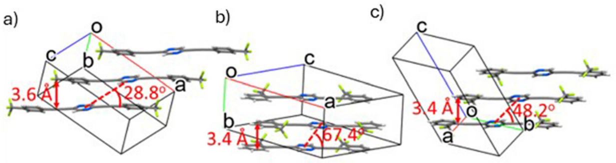

Fig. 8 View of J-aggregates observed along the pyrazine planes for compounds **1a** (a) and **Co-1b** (c). View of the H-aggregate for compound **1b** (b). The slip angle values, and perpendicular distances are also shown.

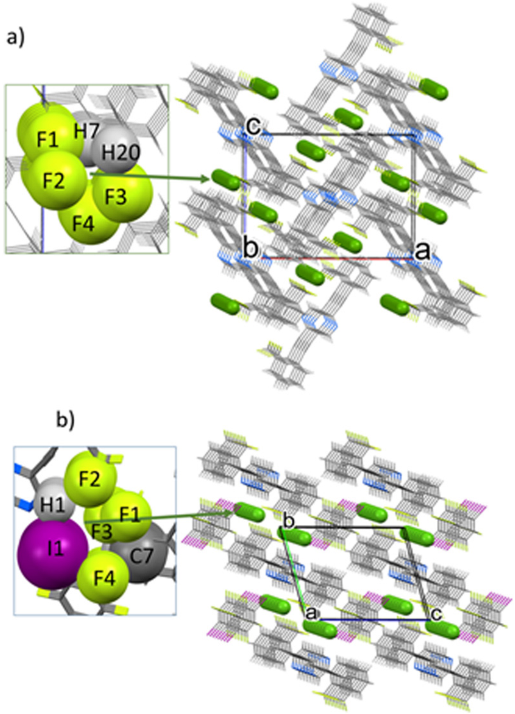

Fig. 9 Representation of microchannels depicted with green balls for compounds (a) **1b** and (b) **Co-1b**. The inset image shows the atoms involved in the channels with their van der Waals radius.

π-stacked manner along the direction of the dipole moment with the slip angle less of 54.7°. Conversely, a face-to-face stacking with a higher angle value would result in H-aggregates.[55]

Taking all these previously described aspects into account, we studied them in the arylethylnyl pyrazine derivatives to gain a deeper understanding of how these parameters influence the behavior of optical waveguides. Analyzing the X-ray diffraction results of the obtained crystals, J-aggregate formation is observed for the *para*-derivatives and the two co-crystals with slip angle values in the range 24.1°–48.2° (Fig. 8 and Fig. S53, ESI†). In contrast, the crystals formed from the *ortho*-substituted derivatives (**1b** and **1d**) pack into H-aggregates with slip angles of 67.4° and 59.6°, respectively. Interestingly, the introduction of a co-assembler induces a change in the crystal structure in compounds **1b** and **1d** that pack into H-aggregates when form part of co-crystals, thus demonstrating that co-crystal formation is a powerful tool for modulating molecular packing and associated properties.

It is noted that the *ortho*-substituted derivatives (**1b** and **1d**) and their co-crystals (**Co-1b** and **Co-1d**) show interplanar distances (3.4–3.5 Å) slightly smaller than those of the *para*-substituted derivatives (3.6–3.8 Å). Thus, this fact may also have an impact on the optical properties, with the *ortho*-derivatives showing better performance as waveguides.

In addition, in a previous article from our group, we established an initial finding that related the presence of internal channels in the crystal structure is concomitant with optical waveguiding behavior. Thus, crystals with internal channels showed waveguiding activity while crystals without them and with compact structures do not behave as optical waveguides.[28] With the aim of delving deeper into this aspect and validating our initial hypothesis, we investigated the presence of microchannels in the crystal structures of the pyrazine derivatives herein reported, including both crystals and co-crystals. It should be noted that all crystals showed infinite microchannels propagated along the direction of the face-to-face molecular array in the same direction as the π-stacking and in the same direction as the growth of the aggregates (Fig. 9 and Fig. S54, ESI†). Obviously, the size and nature of the interactions that form these channels depend on the molecule involved in the self-assembly.

Thus, Fig. 9 shows as an example the presence of microchannels for compounds **1b** and **Co-1b** extend in [010] and [100] directions respectively which coincides with the π-stacking array.

Using the same method as in our previous work, the approximate size of the different microchannels can be determined by defining different average planes containing the edges of the channel and measuring the perpendicular distance of one of the atoms to each of these planes (see Fig. S54, ESI†). The largest microchannel is found in the **Co-1b** structure (4.7 Å and 4.7 Å) and the smallest one in **Co-1d** structure (2.6 Å and 3.1 Å), but the size of these microchannels is of the same order as that published by us for the 2,5-bisethynylbenzene derivatives.[28] In this regard, we hypothesize that, similar to what occurs in tubular waveguides,[59] the presence of air inside the structures could have a beneficial effect on the electric field distribution and light propagation inside the crystals.

The combined analysis of all the results obtained indicates that the six crystals obtained are capable of guiding and transmitting light due to their good crystallinity and structural order. This effect, as described, contributes to the stability of the Frenkel exciton. Additionally, the presence of microchannels in all of them could also contribute to their excellent waveguide properties.

A detailed analysis of the data allows us to conclude that crystals with a 1D structure and short intermolecular distances, which favor orbital overlap (*ortho* derivatives and co-crystals), exhibit better waveguide performance.

Finally, it is worth highlighting that the excellent waveguide properties of crystal **1b** could be attributed not only to the aforementioned characteristics but also to its crystalline structure, which is similar to that of one of the best-described crystals with optical waveguide behavior (BPEA). Moreover, it possesses the highest number of strong directional bonds.

Interaction between the transition dipole moment and the electric field

An important factor in light transmission is the interaction between the molecular transition dipole moment (TDM) and the orientation of the electric field. Transmission efficiency is influenced by the optical loss factor, therefore higher losses result in lower light intensity. While optical loss depends on many factors, among which the presence of defects and inhomogeneities that cause light loss and increase the optical loss coefficient stand out, in active waveguides there are two mechanisms that affect the optical loss coefficient: one from substrate coupling (a_s), which depends on the refractive index and is independent of direction, and another from reabsorption (a_a), which varies with the transmission direction and the orientation of the electric field relative to the TDM. The latter can lead to anisotropic behavior: when polarized light propagates nearly perpendicular to the molecular transition dipole moment, photon–dipole interaction and reabsorption are minimized, resulting in low optical loss and efficient transmission. Conversely, parallel alignment increases photon–dipole interaction, reabsorption, and propagation losses, reducing the light transport efficiency (Fig. S55, ESI†).

In order to deepen the understanding and nature of this interaction, we studied the influence of polarized light on the absorption of the material. Thus, firstly, we have determined computationally the orientation of the $S_0 \rightarrow S_1$ molecular transition dipole moment at the ωB97XD/6-31G** level of theory. The results showed that in all the isolated **1a–1d** molecules the orientation of the molecular TDM is parallel to the largest molecular axis except for **Co-1d** compound where it is almost perpendicular to it (Fig. S56, ESI†). Secondly, the simulation of the crystal morphology was carried out using a BFDH (Bravais–Friedel–Donnay–Harker) method[60,61] which is a reliable method for identifying the most geometrically relevant face in the crystal growth process (red face in Fig. 10 and Fig. S57, ESI†). Finally, the crystals were irradiated with polarized light placing a polarizer in front of the excitation beam path. Fig. 10 and Fig. S58, S59 (ESI†), show how the incident light (black arrow) is perpendicular to the largest surface area of crystal. The red and green arrows and waves indicate the direction of light polarization.

In order to study this effect, the 1D *ortho* derivatives (**1b**, **1d**) were chosen due to their better morphology, and the co-crystal **Co-1d** was selected to examine its impact in a 2D crystal. According to the BFDH law, the face which found to be the largest percentage of area in the crystal is the {101} for compound **1b**, the {011} for compound **1d**, and the {001} for co-crystal **Co-1d**, so it is assumed that this will be the irradiated face in the study of their waveguide properties.

In the case of crystals **1b** and **1d**, there are molecules, marked in blue, that are nearly perpendicular to the irradiated face, with angles of 88.3° for **1b** and 73.2° for **1d**. However, there are also molecules that are practically coplanar with this face, marked in pink, with angles of 15.8° for **1b** and 22.6° for **1d** (Fig. 10a and Fig. S58a, ESI†).

The results show that when light polarization has a longitudinal direction (dashed green arrow) relative to the red face, the electric field is oriented almost perpendicular to the transition dipole moment of the molecules marked in blue and pink, resulting in less light reabsorption and maximum transmission giving rise to the bright crystal edge (Fig. 10c and Fig. S58c, ESI†). In contrast, if the polarization is transversal to the growth face (dashed red arrow), the dipole moments of the molecules marked in pink align almost parallel to the electric field, leading to light reabsorption, and therefore, no luminescence outcoupled from the crystal edge is observed (Fig. 10d and Fig. S58d, ESI†).

Notably, for the 2D co-crystal **Co-1d**, light is transmitted with lower intensity in both directions, whether the light polarization is longitudinal or transversal to the growth face (Fig. S58, ESI†). This phenomenon is due to the transition dipole moments being oriented at angles of 56.3° and 41.6°. In this case, although the angles are smaller than those observed in **1b** and **1d**, they still allow light transmission. However,

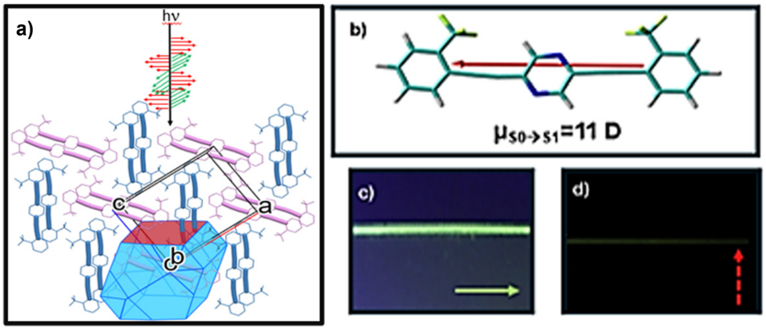

Fig. 10 (a) BFDH model calculated for **1b** crystal. The {101} face with the largest surface area is shown in red color. The orientation of molecular TDM is represented by the atoms of the longest molecular axis shown in capped stick. Black arrow is the incident light. Green vectors and waves indicate the longitudinal direction of polarized light relative to the red face. Red vectors and waves indicate the transversal direction of polarized light relative to the red face. (b) The spatial orientation of the $S_0 \rightarrow S_1$ molecular transition dipole moment for an isolated **1b** molecule, computed at the ωB97XD/6-31G** level of theory. (c) Confocal microscopy image of the transmitted light when the light is polarized in the direction longitudinal to the {101} face (green arrow). (d) Confocal microscopy image of the transmitted light when the light is polarized in the direction transversal to the {101} face (red arrow).

some reabsorption occurs, resulting in reduced transmission intensity.

Of all the compounds studied, it is again evident that derivative **1b** exhibits higher light transmitting efficiency as indicated by the calculated optical loss.

Considering the above, it can be clearly concluded that chemical synthesis is a powerful tool for modulating the geometry and properties of crystals. In this case, small structural variations lead to significant changes in the properties.

Conclusions

This work presents a theoretical and experimental study on the transmission of light through organic structures. For this purpose, 2,5-bis(arylethynyl)pyrazine derivatives with functional groups of different nature in different positions have been synthesized. The synthesis was carried out using Sonogashira coupling reactions and under microwave irradiation as the energy source. These derivatives were self-assembled and co-crystallized with 1,4-diiodotetrafluorobenzene (F_4DIB), resulting in crystals with different morphologies in all cases. All the crystals obtained behave as active waveguides.

An in-depth study of the crystal structures has been conducted. This analysis reveals that the functional groups and their positions play a crucial role in determining the morphology of the crystals. For instance, *para*-substituted derivatives exhibit a similar 2D lamellar packing with a supramolecular organization promoted *via* C–H···π interactions involving the triple bond.

In contrast, the packing of *ortho*-substituted derivatives forms 1D crystals with a herringbone pattern induced by π–π interactions between phenyl groups. On the other hand, the introduction of a co-assembler into the structures enhances the directionality of N···I halogen bonds, which dominate the packing. This causes the hydrogen bonds with the pyrazine to disappear, leading to a displacement of the molecules. As a result, new π···π or C–F···π interactions involving the triple bond emerge, prompting a transition from a herringbone to a 2D lamellar arrangement.

Finally, different structural aspects related to the mechanism and direction of light transmission through these structures were analyzed. The results indicate that well-ordered structures and the presence of microchannels within the crystalline framework contribute significantly to efficient light transmission. Among the key parameters for achieving optimal waveguide behavior are the 1D morphology and short intermolecular distances along the packing direction. Furthermore, it is concluded that the applied field direction and the molecular transition dipole moment should be nearly perpendicular to achieve efficient light propagation.

Among all the crystals studied, crystals of **1b**, which contains $-CF_3$ groups in the *ortho* position, exhibited the best optical waveguide performance. This is attributed not only to the presence of these key characteristics but also to its crystalline structure, which closely resembles that of other crystals with excellent optical waveguide properties, as well as its possession of the highest number of strong directional bonds.

The results of this work highlight that small changes in molecular design can lead to significant differences in the final material, with organic synthesis and co-crystallization serving as powerful tools for achieving these modifications. The knowledge derived from this study is expected to contribute to the custom design of materials with enhanced photonic properties. Future research studies should focus on systematically comparing pure crystals and co-crystals in terms of their optical emission efficiency and mechanical properties. Our results indicate that cocrystals often exhibit enhanced and red-shifted emission due to synergistic intermolecular interactions, while pure crystals may offer greater structural simplicity. To design optical waveguides that are both strongly emissive and flexible, one should consider incorporating co-assemblers that promote robust yet adaptable supramolecular networks. Strategies such as tuning intermolecular interactions to balance rigidity and flexibility, as well as exploring new co-crystallization partners, are promising avenues for achieving these goals.

Author contributions

Irene Chacón-Jiménez: investigation, formal analysis, writing – review & editing. Juan Sánchez-Rincón: investigation, formal analysis, software. Iván Torres-Moya: investigation, formal analysis, writing – review & editing. Berta Gómez-Lor: formal analysis, funding, M. Victoria Gomez: investigation, formal analysis, funding. Juan Cabanillas-González: investigation, formal analysis, funding. M. Carmen Ruíz Delgado: investigation, software, formal analysis, writing, funding. Ana M. Rodríguez: investigation, software, formal analysis, writing – review & editing. Pilar Prieto: investigation, formal analysis, funding, writing – review & editing. The manuscript was written through contributions of all authors. All authors have given approval to the final version of the manuscript.

Conflicts of interest

There are no conflicts to declare.

Data availability

The data collected in this work has not been previously uploaded to any repository. The information has been divided into the following sections: (1) experimental section, (2) ^{1}H-NMR, ^{19}F-NMR, ^{13}C-NMR, ^{1}H–^{1}H COSY-NMR, ^{1}H–^{13}C HSQC-NMR, ^{1}H–^{13}C HMBC-NMR and mass spectra; (3) computational calculations; (4) photophysical characterization; (5) obtention of crystal and co-crystal of 2,5-bis(arylethynyl)pyrazine derivatives; (6) optical waveguides studies; (7) X-ray structure determination for **1a**, **1b**, **1c**, **1d**, **Co-1b** and **Co-1d** and (8) references.

Acknowledgements

This research was funded by the MICINN/AEI/10.13039/501100011033 (Project PID2020-119636GB-I00, PID2023-152323NB-I00, RED2024-153609-T), by the FEDER and Junta de Comunidades de Castilla-La Mancha (JCCM-FEDER) (Project SBPLY/21/180501/000114) and by the University of Castilla-La Mancha (project 2022-GRIN-34310). I. Chacón-Jiménez acknowledges an FPU fellowship (FPU22/01402) of the State Investigation Agency. M. C. R. D. and J. S.-R. acknowledge the funding by MICINN/AEI/10.13039/501100011033 (Project PID2022-139548NB-I00) and by the Junta de Andalucía (FQM-159). J. C.-G. acknowledges the MICINN-FEDER (PID2021-128313OB-I00 and PDC2023-145871-I00), and support from the Regional Government of Madrid (NMAT2D-CM). J. C. G. also acknowledges a Research Consolidation Grant (CNS2022-36191) from the Spanish Ministry of Science and Innovation. IMDEA Nanociencia acknowledges support from the 'Severo Ochoa' Programme for Centres of Excellence in R&D of the Spanish Ministry of Science and Innovation (CEX2020-001039-S). B. G.-L. acknowledges the MICINN/AEI/10.13039/501100011033 (Project PID2023-150022NB-100. The authors would like to thank the SCBI (Supercomputing and Bioinformatics) center of the University of Málaga for providing the computer resources, technical expertise and assistance provided by and Alejandro Martín Merinero for his assistance with fluorescence microscopy. Crystallographic data: CCDC 2386785 (**1a**), 2386786 (**1b**), 2386787 (**Co-1b**), 2386788 (**1c**), 2386789 (**1d**) and 2386790 (**Co-1d**).

Notes and references

1 J. Liu, H. Zhang, H. Dong, L. Meng, L. Jiang, L. Jiang, Y. Wang, J. Yu, Y. Sun, W. Hu and A. J. Heeger, *Nat. Commun.*, 2015, **6**, 1–8.

2 S. Z. Bisri, T. Takenobu, Y. Yomogida, H. Shimotani, T. Yamao, S. Hotta and Y. Iwasa, *Adv. Funct. Mater.*, 2009, **19**, 1728–1735.

3 A. Chetia, J. Bera, A. Betal and S. Sahu, *Mater. Today Commun.*, 2022, **30**, 103224.

4 W. Hourani, K. Rahimi, I. Botiz, F. P. Vinzenz Koch, G. Reiter, P. Lienerth, T. Heiser, J.-L. Bubendorff and L. Simon, *Nanoscale*, 2014, **6**, 4774.

5 B. E. A. Saleh and M. C. Teich, *Fundamentals of photonics*, Wiley, 2019.

6 Y. Ma, Y. Zong, H. Yin, H. Lin, S. Chen and X.-D. Wang, *Adv. Opt. Mater.*, 2021, **9**, 202101481.

7 S. Chen, M.-P. Zhuo, X.-D. Wang, G.-Q. Wei and L.-S. Liao, *Photonix*, 2021, **2**, 2.

8 Y.-L. Shi and X.-D. Wang, *Adv. Funct. Mater.*, 2021, **31**, 2008149.

9 S. Wu, B. Zhou and D. Yan, *Adv. Opt. Mater.*, 2021, **9**, 2001768.

10 W. Ji, B. Xue, S. Bera, S. Guerin, Y. Liu, H. Yuan, Q. Li, C. Yuan, L. J. W. Shimon, Q. Ma, E. Kiely, S. A. M. Tofail, M. Si, X. Yan, Y. Cao, W. Wang, R. Yang, D. Thompson, J. Li and E. Gazit, *ACS Nano*, 2020, **14**, 10704–10715.

11 N. Mitetelo, D. Venkatakrishnarao, J. Ravi, M. Popov, E. Mamonov, T. V. Murzina and R. Chandrasekar, *Adv. Opt. Mater.*, 2019, **7**, 1801775.

12 Z. Ding, H. Shang, Y. Geng, S.-T. Zhang, Z. Huo, Z. Yang, B. Li, W. Xu and S. Jiang, *J. Phys. Chem. Lett.*, 2021, **12**, 4585–4592.

13 M. Annadhasan, S. Basak, N. Chandrasekhar and R. Chandrasekar, *Adv. Opt. Mater.*, 2020, **8**, 2000959.

14 S. Yousuf, J. Mahmoud Halabi, I. Tahir, E. Ahmed, R. Rezgui, L. Li, P. Laws, M. Daqaq and P. Naumov, *Angew. Chem., Int. Ed.*, 2023, **62**, e202217329.

15 L. Lan, L. Li, Q. Di, X. Yang, X. Liu, P. Naumov and H. Zhang, *Adv. Mater.*, 2022, **34**, 2200471.

16 J. Mahmoud Halabi, E. Ahmed, S. Sofela and P. Naumov, *Proc. Natl. Acad. Sci. U. S. A.*, 2021, **118**, e2020604118.

17 C. B. Aakeröy and D. J. Salmon, *CrystEngComm*, 2005, **7**, 439.

18 F. Wöhler, *Annal*, 1844, **51**, 153.

19 G. R. Desiraju, *CrystEngComm*, 2003, **5**, 466.

20 J. D. Dunitz, *CrystEngComm*, 2003, **5**, 506.

21 P. Yu, Y. Zhen, H. Dong and W. Hu, *Chem*, 2019, **5**, 2814–2853.

22 W. Zhu, R. Zheng, Y. Zhen, Z. Yu, H. Dong, H. Fu, Q. Shi and W. Hu, *J. Am. Chem. Soc.*, 2015, **137**, 11038–11046.

23 J. Perlstein, *Chem. Mater.*, 1994, **6**, 319–326.

24 W. Zhu, L. Zhu, Y. Zou, Y. Wu, Y. Zhen, H. Dong, H. Fu, Z. Wei, Q. Shi and W. Hu, *Adv. Mater.*, 2016, **28**, 5954–5962.

25 X.-H. Ding, Y.-Z. Chang, C.-J. Ou, J.-Y. Lin, L.-H. Xie and W. Huang, *Natl. Sci. Rev.*, 2020, **7**, 1906–1932.

26 Y. Yan and Y. S. Zhao, *Adv. Funct. Mater.*, 2012, **22**, 1330–1332.

27 P. Lova, V. Grande, G. Manfredi, M. Patrini, S. Herbst, F. Würthner and D. Comoretto, *Adv. Opt. Mater.*, 2017, **5**, 201700523.

28 C. Tardío, J. Álvarez-Conde, I. Torres-Moya, A. M. Rodríguez, A. de la Hoz, J. Cabanillas-González and P. Prieto, *J. Mater. Chem. C*, 2022, **10**, 6411–6418.

29 C. Zhang, C.-L. Zou, Y. Yan, R. Hao, F.-W. Sun, Z.-F. Han, Y. S. Zhao and J. Yao, *J. Am. Chem. Soc.*, 2011, **133**, 7276–7279.

30 Y. Liu, H. Hu, L. Xu, B. Qiu, J. Liang, F. Ding, K. Wang, M. Chu, W. Zhang, M. Ma, B. Chen, X. Yang and Y. S. Zhao, *Angew. Chem.*, 2020, **132**, 4486–4493.

31 Q. H. Cui, Q. Peng, Y. Luo, Y. Jiang, Y. Yan, C. Wei, Z. Shuai, C. Sun, J. Yao and Y. S. Zhao, *Sci. Adv.*, 2018, **4**, 9861.

32 C.-F. Ng, H.-F. Chow and T. C. W. Mak, *CrystEngComm*, 2019, **21**, 1130–1136.

33 K. Lisac, V. Nemec, F. Topić, M. Arhangelskis, P. Hindle, R. Tran, I. Huskić, A. J. Morris, T. Friščić and D. Cinčić, *Cryst. Growth Des.*, 2018, **18**, 2387–2396.

34 V. Vinay Pradeep, C. Tardío, I. Torres-Moya, A. M. Rodríguez, A. Vinod Kumar, M. Annadhasan, A. de la Hoz, P. Prieto and R. Chandrasekar, *Small*, 2021, **17**, 2006795.

35 D. Iglesias, R. Martín, M. Á. Álvarez-Sánchez, I. Badía-Domínguez, E. Vázquez, M. Carmen Ruiz Delgado, P. Prieto and M. Antonia Herrero, *Nanoscale*, 2023, **15**, 12280–12286.

36 R. S. Varma, *ACS Sustainable Chem. Eng.*, 2016, **4**, 5866–5878.

37 S. Tiwari and S. Talreja, *J. Pharm. Res. Int.*, 2022, 74–79.

38 A. De la Hoz, A. Díaz-Ortiz and P. Prieto, *Microwave-Assisted Green Organic Synthesis, Alternative Energy Sources for Green Chemistry*, Springer, Berlín, 2016, vol. 1.

39 M. J. Pastor, I. Torres, C. Cebrián, J. R. Carrillo, Á. Díaz-Ortiz, E. Matesanz, J. Buendía, F. García, J. Barberá, P. Prieto and L. Sánchez, *Chemistry*, 2015, **21**, 1795–1802.

40 I. Torres, A. Díaz-Ortiz, L. Sánchez, J. Orduna, M. J. Blesa, J. R. Carrillo and P. Prieto, *Dyes Pigm.*, 2017, **142**, 212–225.

41 S. Kothavale and N. Sekar, *Dyes Pigm.*, 2017, **136**, 31–45.

42 A. Marini, A. Muñoz-Losa, A. Biancardi and B. Mennucci, *J. Phys. Chem. B*, 2010, **114**, 17128–17135.

43 E. Gagnière, D. Mangin, F. Puel, A. Rivoire, O. Monnier, E. Garcia and J. P. Klein, *J. Cryst. Growth*, 2009, **311**, 2689–2695.

44 D. Yan, H. Yang, Q. Meng, H. Lin and M. Wei, *Adv. Funct. Mater.*, 2014, **24**, 587–594.

45 S. Li and D. Yan, *Adv. Opt. Mater.*, 2018, **19**, 201800445.

46 M.-P. Zhuo, J.-J. Wu, X.-D. Wang, Y.-C. Tao, Y. Yuan and L.-S. Liao, *Nat. Commun.*, 2019, **10**, 1–9.

47 S. Militzer, T. M. P. Tran, P. J. Mésini and A. Ruiz-Carretero, *ChemNanoMat*, 2018, **4**, 790–795.

48 G. Martinez, N. R. Ávila-Rovelo, C. C. Carmona-Vargas, I. Idboubrik and A. Ruiz-Carretero, *Eur. J. Org. Chem.*, 2023, 26.

49 M. Annadhasan, D. P. Karothu, R. Chinnasamy, L. Catalano, E. Ahmed, S. Ghosh, P. Naumov and R. Chandrasekar, *Angew. Chem., Int. Ed.*, 2020, **59**, 13821–13830.

50 Z. Lu, Y. Zhang, H. Liu, K. Ye, W. Liu and H. Zhang, *Angew. Chem., Int. Ed.*, 2020, **59**, 4299–4303.

51 H. Liu, Z. Lu, Z. Zhang, Y. Wang and H. Zhang, *Angew. Chem., Int. Ed.*, 2018, **57**, 8448–8452.

52 M.-P. Zhuo, Y.-C. Tao, X.-D. Wang, Y. Wu, S. Chen, L.-S. Liao and L. Jiang, *Angew. Chem., Int. Ed.*, 2018, **57**, 11300–11304.

53 M.-P. Zhuo, Y.-C. Tao, X.-D. Wang, S. Chen and L.-S. Liao, *J. Mater. Chem. C*, 2018, **6**, 9594–9598.

54 R. Martín, A. Sánchez-Oliva, A. Benito, I. Torres-Moya, A. M. Garcia, J. Álvarez-Conde, J. Cabanillas-González, P. Prieto and B. Gómez-Lor, *J. Mater. Chem. C*, 2024, **12**, 2903–2910.

55 S. Ma, S. Du, G. Pan, S. Dai, B. Xu and W. Tian, *Aggregate*, 2021, **4**, 2.

56 F. C. Spano, *Acc. Chem. Res.*, 2010, **43**, 429–439.

57 D. Chaudhuri, D. Li, Y. Che, E. Shafran, J. M. Gerton, L. Zang and J. M. Lupton, *Nano Lett.*, 2011, **11**, 488–492.

58 R. Schäfer, L. Böhner, M. Schiek, D. Hertel, K. Meerholz and K. Lindfors, *ACS Photonics*, 2024, **11**, 111–120.

59 Y. S. Zhao, J. Xu, A. Peng, H. Fu, Y. Ma, L. Jiang and J. Yao, *Angew. Chem., Int. Ed.*, 2008, **47**, 7301–7305.

60 J. D. H. Donnay and D. Harker, *Am. Min.*, 1937, **22**, 446.

61 R. F. P. Grimbergen, H. Meekes, P. Bennema, C. S. Strom and L. J. P. Vogels, *Acta Crystallogr., Sect. A: Found. Crystallogr.*, 1998, **54**, 491–500.